Ionospheric Chaos in Solar quiet Current due to Sudden Stratospheric Warming Events Across Europe-Africa Sector

Irewola Aaron, Oludehinwa[1,2,*]; Andrei, Velichko[3]; Olasunkanmi Isaac, Olusola[2]; Olawale Segun, Bolaji[3,6]; Norbert, Marwan[4]; Babalola Olasupo, Ogunsua[5,7]; Abdullahi Ndzi, Njah[2]; Timothy Oluwaseyi Ologun[7].

1. Department of Physics, Caleb University, Lagos, Nigeria
2. Department of Physics, University of Lagos, Lagos, Nigeria
3. Institute of Physics and Technology, Petrozavodsk State University, 185910 Petrozavodsk, Russia.
4. Research Department of Complexity Science, Potsdam Institute for Climate Impact Research (PIK), Member of the Leibniz Association, 14412 Potsdam, Germany.
5. Key Laboratory for middle Atmospheric and Global Environment Observation (LAGEO), Institute of Atmospheric Physics (IAP), Chinese Academy of Science, Beijing, China.
6. Department of Physics, University of Tasmania, Australia.
7. Department of Physics, Federal University of Technology, Akure, Nigeria.

*Corresponding-Author:
irewola.oludehinwa@calebuniversity.edu.ng; or Irewola2012@yahoo.com
Tel.: +2348068030109

Abstract

This study examines the ionospheric chaos in the solar quiet current, $S_q(H)$ across Europe and Africa sectors during 2009 and 2021 Sudden Stratospheric Warming (SSW) events. The SSW was categorized into precondition, ascending, peak, descending, after and no-SSW phases based on the rising stratospheric temperature. Thirteen magnetometer stations, located within the geographical longitude of 26° to 40° across Europe and Africa sectors were considered. The magnetometer data obtained during the periods of SSW were used to derived the solar quiet current time series. This solar quiet current time series was transformed into a complex network using the HVG approach, and Fuzzy Entropy was applied to the resulting node-degree time series to quantify the presence of chaos or orderliness behavior in the ionosphere during SSW. The results revealed that the latitudinal distribution of entropy in Europe sector depicts high entropy values indicating the presence of ionospheric chaos. Consistent low entropy values unveiling the presence of orderliness

behavior were found to be prominent in the Africa sector. This dominance of orderliness behavior during the phases of SSW in the Africa sector reveal that SSW effect manifest orderliness behavior on the regional ionosphere of Africa sector. While, the pronounced features of ionospheric chaos found in the European sector reveal evidence of significant effects of SSW on the regional ionosphere in this sector. Finally, we found that after the peak phase of SSW, the ionospheric chaos is more pronounced.

Keywords: Sudden Stratospheric Warming (SSW), Solar quiet current $S_q(H)$, Ionospheric chaos, Fuzzy Entropy, Horizontal Visibility Graph (HVG

1. Introduction.

The chaotic behavior of the ionosphere dominates due to the complex interaction between the lower and upper atmospheric circulation. This complex interaction is influenced by geographical location, solar activity, and atmospheric dynamics. One of the lower atmospheric events capable of causing global disruptions to the ionosphere is Sudden Stratospheric Warming (SSW). SSW is one of the usual meteorological events, where the stratospheric temperature increases rapidly in the winter polar region due to the rapid growth of quasi-stationary planetary waves from the troposphere (Baldwin et al., 2021; Butler et al., 2015). The connections between the troposphere and stratosphere during SSW introduces upward wave energy propagation that can reshape the plasma density variability in the ionosphere. The dominant mechanism facilitating the connection of these processes include planetary waves, atmospheric tides, and gravity waves (Goncharenko et al., 2021; Chau et al., 2012; Goncharenko et al., 2010, 2012; Liu et al., 2010). Also, other external sources that could facilitates SSWs are Heliospheric Plasma Sheet (HPS) and magnetosphere interaction. This occur when HPS impinges on the magnetosphere, compressing it and accelerates protons, which in turn generate Electromagnetic Ion Cyclotron (EMIC) waves.

These waves interact with relativistic electrons, causing their rapid loss to the atmosphere, potentially affecting climate mechanism (Tsurutani et al., 2016; Liu et al., 2022)

The SSW effect introduces spatial and temporal variability in the ionospheric plasma density (Yamazaki, 2013, 2014; Klimenko et al., 2018). As a result, the ionosphere exhibits nonlinear dynamical behavior, characterized by high sensitivity to minor perturbations originating from the lower and upper atmosphere that could lead to transitions between orderliness and chaotic behavior of ionosphere, rendering its state susceptible to sudden and significant changes.

In the studies of dynamical systems such as logistic map, chaotic behavior is strongly associated with high entropy measures while orderliness behavior is associated with a declining and low entropy measures (Conejero et al., 2024). This observation forms the basis of this study, to quantitatively examine the dynamical behavior of the ionosphere during SSW across European and African sector. The regional ionosphere of European and Africa sectors manifest pronounced ionospheric variability in response to SSW events. For example, proximity to the geomagnetic equator in Africa could lead to different responses compared to higher latitude regions in Europe. This phenomenon provides a unique opportunity to investigate the complex coupling mechanisms between the stratosphere and ionosphere. Specifically, it enables the study of atmospheric wave propagation and its impact on the ionosphere, which can lead to disruptions in satellite communication and navigation system in the region.

One of the atmospheric parameters that can reveal the extent of the SSW-induced effects on the regional ionosphere is the solar quiet current, $S_q(H)$. During SSW event, planetary waves and tidal interactions can generate an electromotive force that drives the ionospheric current system (Yamazaki and Richmond, 2013; Yamazaki and Maute, 2017). These ionospheric currents during

77 geomagnetically quiet periods are referred to as Solar quiet currents (S_q). They serve as a key
78 phenomenon that manifest the degree of connection between the lower atmosphere and the
79 ionosphere.

80 Several studies have already investigated the solar quiet current during SSW (Yamazaki, 2014;
81 Bolaji et al., 2016a; Yamazaki and Maute, 2017; Yamazaki et al., 2011). For instance, Fejer et al.
82 (2011) found enhanced lunar semi-diurnal vertical plasma drift amplitudes during early morning
83 solar flux warming, associated with SSW. Maute et al. (2014) observed changes in ionospheric
84 vertical drifts during SSW, attributing them to interactions between specific tides and planetary
85 waves. Yamazaki et al. (2012a) studied the ionospheric current system during the 2002-2003 SSW
86 events over East Asia, finding an additional current system superposed on the normal Sq current
87 system. They attributed this to abnormally large lunar tidal winds, which also produced a counter
88 electrojet (CEJ). Yamazaki et al. (2012b) examined the solar quiet current during SSW, finding
89 significant hemispheric asymmetry: decreased intensity in the Northern Hemisphere and increased
90 intensity in the Southern Hemisphere, accompanied by reduced longitudinal separation between
91 the hemispheric eddies. Yamazaki, (2014) studied the solar and lunar ionospheric tidal forces,
92 which are believed to influence ionospheric electrodynamics during SSW. By analyzing the
93 average solar and lunar ionospheric current systems during SSW and non-SSW periods, he
94 discovered that the intensity of lunar currents increases by roughly 75% during SSWs, whereas
95 the solar current intensity is only slightly diminished, by approximately 10%. Bolaji et al. (2016b)
96 investigated the solar quiet current response in Africa during SSW, categorizing temperature rises
97 into six phases. A counter electrojet formed after peak SSW, and Sq(H) magnitude decreased
98 between 21.13°N (Fayum, Egypt) and 39.51°S (Durban, South Africa) was observed. Siddiqui et
99 al. (2018) examined the Equatorial Electrojet (EEJ) during major SSW events, finding a significant

increase in the amplitude of EEJ semidiurnal lunar tides during SSW. Klimenko et al. (2019) investigated the impact of the 2009 SSW on the tropical lower thermosphere-ionosphere. They found that perturbations in ionospheric conductivity significantly contribute to the electric field response to SSW. Additionally, the phase change of the semidiurnal solar tide (SW2) in neutral winds played a crucial role in shaping the zonal electric field response.

Interestingly, previous studies on solar quiet currents during SSW events have not consider the application of chaos theory. This study aims to bridge this gap by investigating the chaotic behavior of the solar quiet current system in response to SSW effects over the European and African sectors. To examine the ionosphere during 2009 and 2021 SSW events, this study utilizes a robust methodology combining two innovative techniques: the Horizontal Visibility Graph (HVG), rooted in graph theory, to preprocess solar quiet current time series data, and Fuzzy Entropy (FuzzyEn) analysis to reveal the underlying chaotic behavior in the ionosphere during SSW. The reason why this study considers the combination of HVG and Fuzzy Entropy techniques is that Fuzzy Entropy is indeed robust to small-amplitude noise, some subtle features in the solar quiet current time series may still be obscured if we rely on FuzzyEn alone. The HVG transformation helps by emphasizing the "visibility" relations between data points effectively highlighting structural patterns that may be drowned out in the raw time series. In addition, when FuzzyEn is computed on node-degree sequence (complex network representation), it often provides clearer differentiation of regimes or subtle changes in the system that might otherwise remain hidden. Thus, the combined HVG and FuzzyEn approach can yield features more robust to measurement noise and more sensitive to underlying structural variations in the solar quiet current.

1.1 Characterization of 2009 and 2021 Major SSW Events

The 2009 SSW event occurred from January to March. Its rising stratospheric temperature and the corresponding stratospheric zonal mean wind was categorized into six phases during these periods: SSW Pre-Condition Phase, SSW Ascending Phases, SSW Peak Phase, SSW Descending Phase, After SSW Phase, and No SSW phase (Figure (1)). The red color represents the stratospheric mean air temperature (k) at 10hPa. While the black color is the stratospheric zonal mean wind at 10hPa.

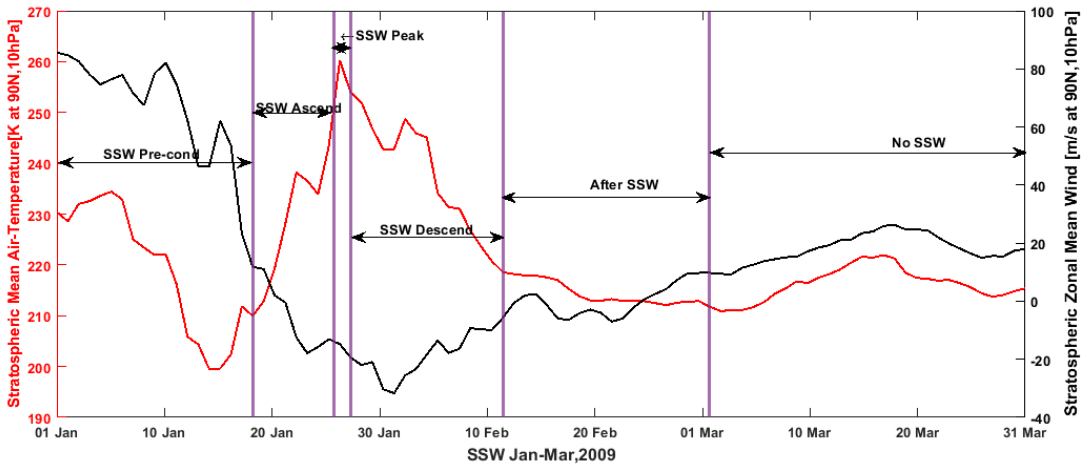

Figure 1: The stratospheric zonal mean air temperature and zonal mean wind occurring January-March, 2009 showing the SSW Precondition Phase, SSW Ascending Phase, SSW peak Phase, SSW Descending Phase, After SSW Phase and no SSW phase. The stratospheric parameter during the 2009 SSW event is obtained from the National Oceanic and Atmospheric Administration (NOAA).

The SSW precondition phase represents the start of the increase in the stratospheric temperature (1-16 January) shown in Figure 1, the SSW ascending phase signifies when the stratospheric temperature increases (17-21 January), the SSW peak phase is when the stratospheric temperature reaches its maximum (22-24 January), the SSW Descending phase indicates the begin of the

stratospheric temperature decline (25 January-12 February), the After SSW phase represents when the stratospheric temperature begins to recover to its normal state (13 February-2 March), and the No SSW phase represents when the stratospheric temperature finally recovers to its normal state (3-31 March). The SSW event was categorized in accordance to the work of (Bolaji et al., 2016b).

The stratospheric temperature and its corresponding zonal mean wind for the 2021 SSW event is shown in Figure 2. The SSW occurred from December 2020 to February 2021 and was also categorized into six phases. The SSW precondition phase spans between 1 and 27 December, 2020, the SSW ascending phase is from 28 December 2020 to 2 January 2021, while the SSW peak phase ranges from 3-5 January 2021, the SSW descending phase spans within 6-14 January 2021, and the After-SSW phase is from 15 January-16 February 2021. Finally, the No SSW phase emerges from 17-28 February 2021.

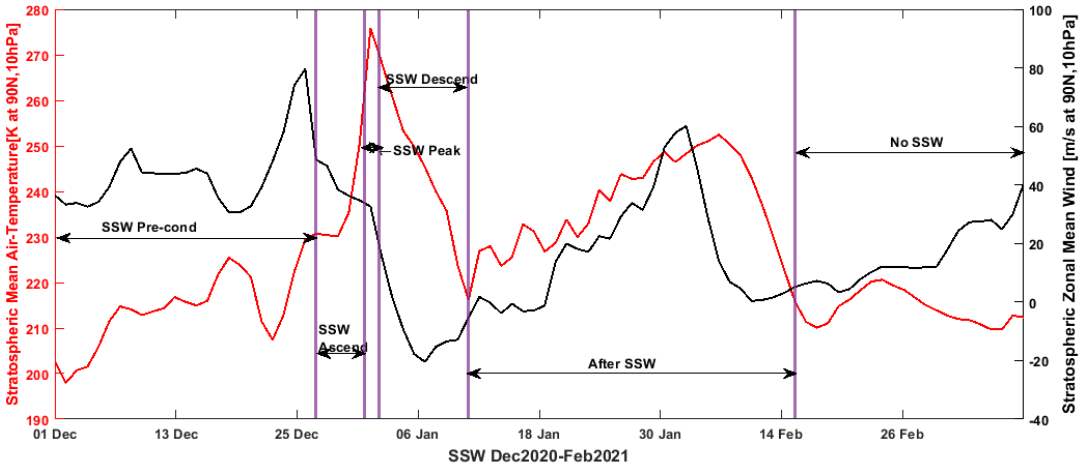

Figure 2: The stratospheric zonal mean air temperature and zonal mean wind from December 2020 until February, 2021 revealing the SSW Precondition Phase, SSW Ascending Phase, SSW peak Phase, SSW Descending Phase, After SSW Phase and no SSW phase. The stratospheric parameter

154 during the 2021 SSW event is obtained from the National Oceanic and Atmospheric
155 Administration (NOAA).

156 **1.2 Global Scale of geomagnetic activities during the 2009 and 2021 SSW Events**

157 The year 2009 was the beginning of a solar minimum of the solar cycle 24 while the year 2021
158 was the end of solar minimum in the solar cycle 24. Generally, solar minimum years are periods,
159 where the geomagnetic disturbances mostly record quiet days. This indicates that the years 2009
160 and 2021 of solar cycle 24 are periods where the geomagnetic disturbances were mostly minimal.
161 The planetary index (K_p) and the solar flux activity during the months of 2009 and 2021 SSW
162 event are shown in Figures (3 & 4) respectively. During the 2009 SSW event (January-March), the
163 planetary K_p index generally depicts quiet geomagnetic conditions ($K_p \leq 3$) for most days, as
164 shown in Figure 3. However, there were 11 exceptions (January 3, 19, 26, February 4, 14-15, 25,
165 28, March 13, and 24) where K_p index values slightly exceeded 3 noticed within the 3-hr interval
166 range of K_p indicating sudden occurrence of moderate geomagnetic disturbance.

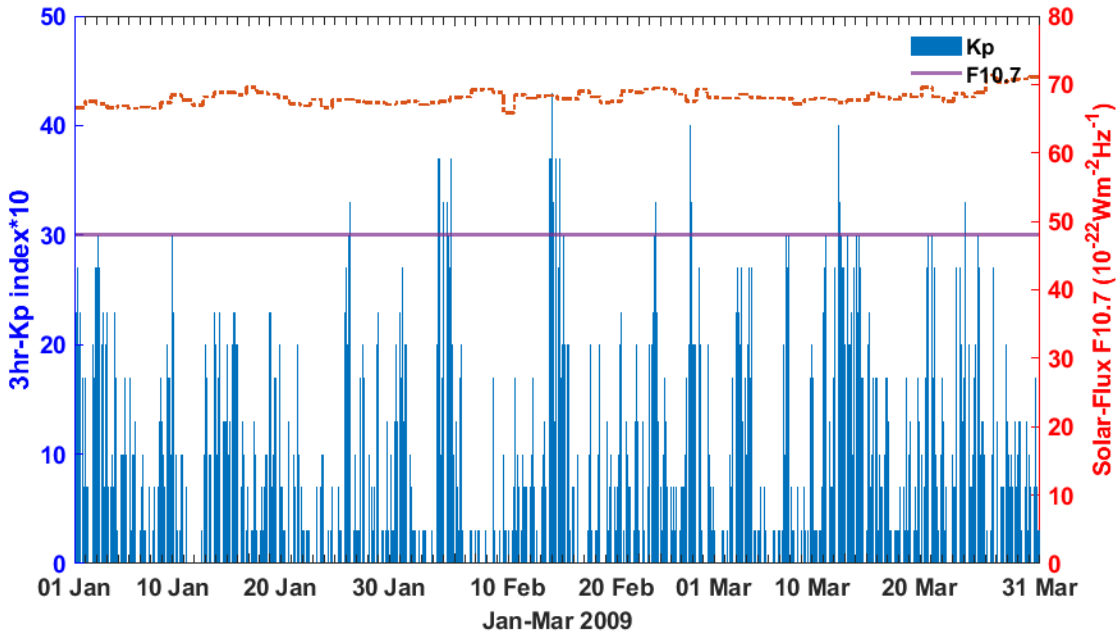

167

Figure 3: The planetary index K_p (blue bars) and Solar flux $F_{10.7}$ (red lines) between January to March, 2009. The planetary (K_p) and Solar flux activity ($F_{10.7}$) during 2009 SSW periods collected from the Space Physics Data Facility, NASA.

The planetary K_p index during the 2021 SSW event (December 2020 to February 2021), as shown in Figure 4, generally indicated quiet geomagnetic conditions ($K_p \leq 3$) for most days and the solar flux activity was within $F_{10.7}$~100. However, elevated K_p index values (> 3) were observed on 17 specific days (December 10, 21, 23, January 5, 6, 11, 24, 25, 27, February 2, 6, 12, 16, 20, 22, 23). Because to this sudden occurrence of transient geomagnetic disturbance revealed by the K_p index in the amentioned days during the SSW periods. In our analysis of solar quiet current derivation, we ensure that geomagnetic storm index in minutes (SYM-H) was subtracted from the H-component of the magnetic field to minimize the influence of geomagnetic disturbance. However, a comparative analysis of the day-to-day geomagnetic activity in January-March, 2009 and December 2020-February 2021 SSW events reveals that most days during these periods manifest K_p index values ≤ 3, indicating minimal geomagnetic activity. This observed space weather feature underscores the uniqueness of the selected SSW events for this study. An investigation into the chaotic behavior of the ionosphere during periods of low geomagnetic activity of SSW will reveal the significant impact of SSW events on ionospheric dynamics within the European and African sectors.

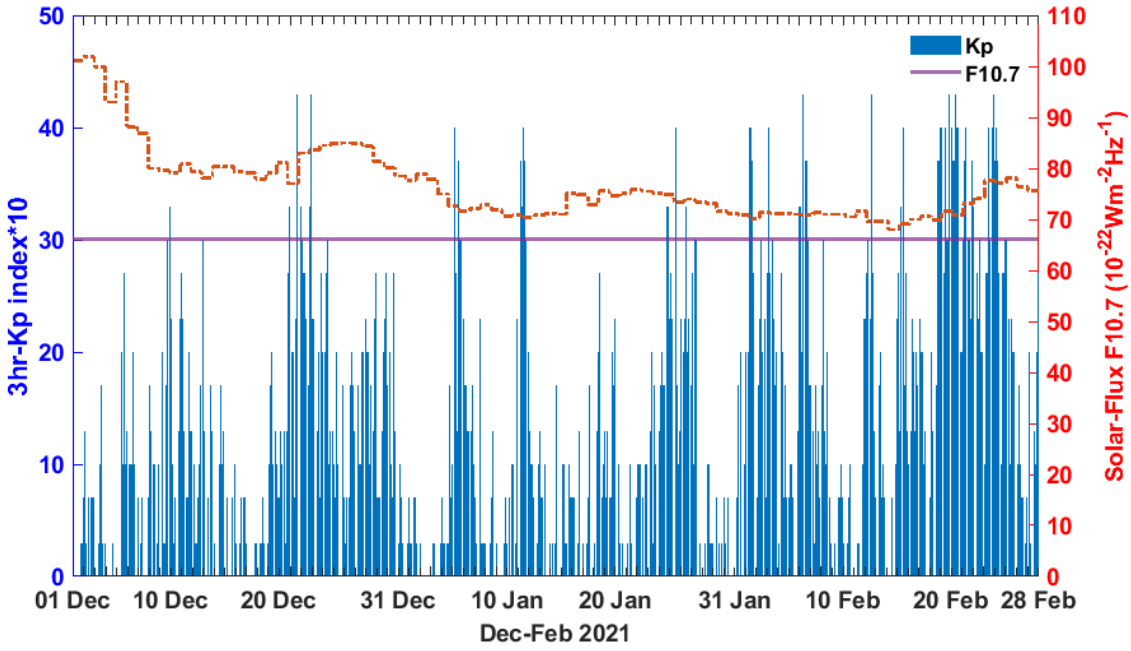

Figure 4: The planetary index: K_p (blue bar) and Solar flux $F_{10.7}$ (red lines) from December 2020-February, 2021. The planetary (K_p) and Solar flux activity ($F_{10.7}$) during 2021 SSW periods collected from the Space Physics Data Facility, NASA

2. Data Acquisition and Method of Analysis

The ground-based magnetometer data acquired from the Magnetic Data Acquisition System (MAGDAS) at the International Research Centre for Space and Planetary Environment Science ($i-SPES$), Fukuoka, Japan (http://magdas2.serc.kyushu-u.ac.jp/) was used in this study. The geographical location of the studied areas is shown in Figure 5.

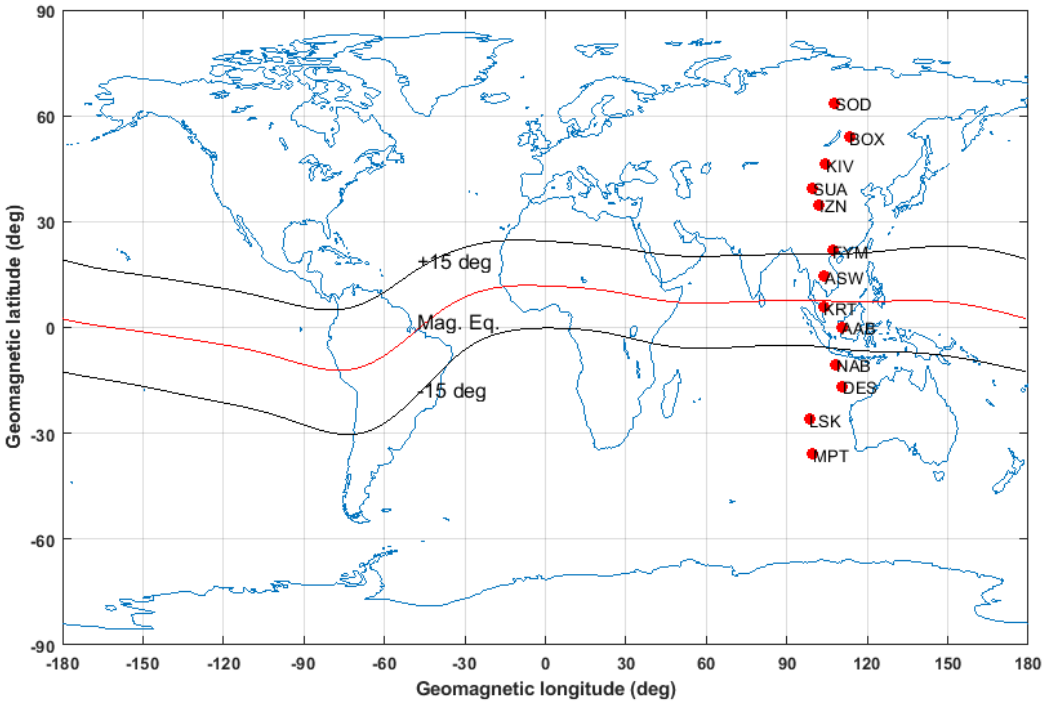

195

196 Figure 5: The geomagnetic location of the magnetometer observatories stations investigated across

197 the Europe and Africa sector.

198 The acquired magnetic data from MAGDAS covers 8 magnetometer stations situated in the Africa

199 sector distributed within the geographical latitudes of both Northern and Southern Hemisphere

200 shown in Table 1. The geomagnetic coordinate reference year for the stations listed in Table 1 is

201 2009.

202 **TABLE 1: STATIONS INVESTIGATED ACROSS EUROPE AND AFRICA SECTOR**

S/ No	Stations	Country	Geographical latitude	Geographical Longitude	Geomagnetic Latitude	Geomagnetic Longitude	Local Time (LT)	Magnetometer Network
1	Sodankyla (SOD)	Finland	67.37	26.63	63.70	107.68	UTC+3	INTERMAGNET
2	Borok (BOX)	Russia	58.07	38.23	53.92	113.32	UTC+3	INTERMAGNET
3	Kiev Dymer (KIV)	Ukraine	50.70	30.30	46.32	104.39	UTC+3	INTERMAGNET
4	Surlari (SUA)	Romania	44.68	26.25	39.52	99.52	UTC+3	INTERMAGNET
5	Iznik (IZN)	Turkey	40.50	29.72	34.74	102.13	UTC+3	INTERMAGNET
6	Fayum (FYM)	Egypt	29.18	35.50	21.78	106.00	UTC+2	MAGDAS

7	Aswan (ASW)	Egypt	23.50	32.51	14.56	103.89	UTC+2	MAGDAS
8	Khartoum (KRT)	Sudan	15.33	32.32	5.69	103.80	UTC+2	MAGDAS
9	Addis Ababa (AAB)	Ethiopia	9.01	38.74	0.14	110.44	UTC+3	MAGDAS
10	Nairobi (NAB)	Kenya	-1.10	36.48	-10.58	108.18	UTC+3	MAGDAS
11	Dar es Salaam (DES)	Tanzania	-6.80	39.28	-16.62	110.72	UTC+3	MAGDAS
12	Lusaka (LSK)	Zambia	-15.23	28.19	-26.06	98.31	UTC+2	MAGDAS
13	Maputo (MPT)	Mozambique	-25.50	32.36	-35.92	99.56	UTC+2	MAGDAS

Also, magnetometer stations in the Europe were acquired from the International Real-time Magnetic Observatory Network (INTERMAGNET), available online at www.intermagnet.org. The collection consists of 5 magnetometer observatory stations across Europe, see Table 1. The magnetometer data were acquired during the periods of the 2009 and 2021 SSW events. Owing to lack of magnetic data at geographical longitude between 26^0 and 40^0 in Africa sector, during 2021 SSW, our study of 2021 SSW was restricted only to European sector.

The planetary (K_p) index during 2009 and 2021 SSW periods was downloaded from GFZ Indices of Global Geomagnetic Activity (https://www.gfz-potsdam.de/Kp-index/) while the Solar flux activity ($F_{10.7}$) at 2009 and 2021 SSW periods were collected online from the archive of the Space Physics Data Facility, NASA (https://omniweb.gsfc.nasa.gov/form/dx1.html).

The daily mean values of zonal mean air temperature and wind during the periods of 2009 and 2021 SSW were acquired from the National Oceanic and Atmospheric Administration (NOAA) (https://psl.noaa.gov/data/getpage/). The solar quiet currents, $S_q(H)$, was derived using the H-component of the magnetic field data with daily resolution (with time unit in minutes). A magnetic field model (CHAOS-8.1), spanning 1999-2025, was obtained from DTU Space (https://www.space.dtu.dk/english/research/scientific_data_and_models/magnetic_field_models) to determine the ionospheric field. CHAOS-8.1 is derived from magnetic field observations by

low-Earth orbiting satellites (Swarm, MSS-1, CSES, CryoSat-2, CHAMP, SAC-C, and Ørsted) and ground observatory measurements.

2.1 Derivation of Solar quiet Current $S_q(H)$ time Series

To derive the day-to-day $S_q(H)$ current time series, magnetic field data from various magnetometer stations across European and Africa sector were archived. We focus on acquiring magnetic field data from the magnetometer stations that are situated within the geographical longitude (26°-40°). Some of the acquired magnetic data, especially the stations in Europe sector are provided in Cartesian (X, Y, Z) coordinate system, and was converted to geomagnetic (H, D, Z) coordinate system using Rotation Matrix method (Barton and Tarlowski, 1991). We applied a magnetic field model (CHAOS-8.1) with the acquired magnetic field data to obtain the ionospheric field. The H-component of the magnetic field model (CHAOS) was subtracted from the H-component of the acquired magnetic data.

$$\Delta H = \Delta H_{magnetic\ data} - \Delta H_{model} \quad (1)$$

To minimize the disturbance field arising from the magnetospheric currents (Bolaji et al., 2016b). The values of the geomagnetic storm index in minutes (SYM-H) were subtracted from the H-component (ΔH).

$$\Delta H_{local} = \Delta H - (SYM - H \times \cos(L)) \quad (2)$$

To estimate the solar quiet current $S_q(H)$ time series, the average nighttime values (in minutes) of the H-component between 24:00 and 1:00 local time (LT) for a particular day refers as Baseline Value (BLV) was estimated using equation (3).

$$BLV = \frac{\Delta H_{24} + \Delta H_{01}}{2} \quad (3)$$

242 The notation ΔH_{24} and ΔH_{01} are the 60 minutes values of H component at 24:00 and 01:00 LT
243 respectively. Where BLV represent the Baseline line value. The residual value after subtracting the
244 baseline value from the H-component gives rise to the solar quiet current time series.

245 $$S_q(H) = \Delta H_{local} - BLV \quad (4)$$

246 Where $S_q(H)$ is the solar quiet current considered in minutes. The analysis of the $S_q(H)$ was
247 deduced for all the day-to-day activities of the 2009 SSW (January-March) and 2021 SSW
248 (December 2020-Februay) periods for all stations under investigation.

249 **2.2 Detrending of Solar quiet Sq(H) Current Time Series by Horizontal Visibility Graph**
250 **(HVG).**

251 The time series of the solar quiet current. Sq(H) derived during the periods of the 2009 and 2021
252 SSW was subjected to the HVG method which transform the series into a complex network. The
253 calculations were performed using the ts2vg Python module, specifically utilizing the
254 HorizontalVG class, which represents one of the types of visibility graphs, namely the 'Horizontal
255 Visibility Graph'. The input to this process is a time series, which is transformed into a network
256 where each point in the series becomes a node, and edges are formed based on the visibility criteria
257 between points (Conejero et al., 2024; Gonçalves et al., 2016; O'Pella, 2019; Luque et al., 2009;
258 Zou et al., 2019). By applying this method, we calculate the degree (number of connections) for
259 each point in the time series, capturing the number of other points it can 'see' in the horizontal
260 visibility graph. The output is a list of degrees for each point, reflecting the local connectivity
261 structure within the time series, which helps reveal patterns, dependencies, and variability within
262 the data. The HVG is mathematically described as follows:

263 Let us consider a time series of *N*-data points be represented as:

$$[x_i, i = 1,2, \dots, N] \quad (5)$$

Two nodes i and j in the graph are connected, if it is possible to trace a horizontal line in the series linking x_i and x_j not intersecting intermediate data height, fulfilling:

$$x_i, x_j > x_n \text{ for all } i < n < j \quad (6)$$

2.3 Fuzzy Entropy (FuzzyEn)

Fuzzy Entropy (FuzzyEn) is a powerful and popular nonlinear tool used to assess the dynamical characteristics of time series data (Ishikawa and Mieno, 1979; Li et al., 2017; Azami et al., 2019; Chen et al., 2007). It provides a quantitative measure of a signal's complexity and chaos. High entropy indicates a more irregularity (chaotic) dynamics, whereas low entropy suggests a more regular or periodic nature. FuzzyEn was developed to overcome the shortcoming of approximate entropy (ApEn) and sample entropy (SampEn), (Azami et al., 2019; Li et al., 2017; Dass et al., 2019). FuzzyEn uses exponential functions with Fuzzy boundaries. It is expressed mathematically as follows. Given a time series, we embed it using a given embedding dimension (m). Then, a new m-dimensional vector (X_m) is formed as

$$X_m(i) = [X_i, X_{i+1}, \dots, X_N] - x0_i \quad (7)$$

These vectors represent m consecutive x-values, starting with the i-th points, and with the baseline $x0_i = \frac{1}{m}\sum_{j=0}^{m-1} x_{i+j}$ removed. Then, the distance between vectors $X_m(i)$ and $X_m(j)$, $d_{i,j,m}$ can be defined as the maximum absolute difference between their scalar components. Given n and r, the degree of similarity $(D_{i\ j,m})$ of the vectors $X_m(i)$ and $X_m(j)$ is calculated using the fuzzy function:

$$D_{i,j,m} = \mu\left(d_{i,j,m}, r\right) = exp\left(\frac{-(d_{i,j,m})^n}{r}\right) \quad (8)$$

Where n and r are the FuzzyEn power and threshold respectively. The function ϕ_m is defined as

$$\phi_m(n,r) = \frac{1}{N-m}\sum_{i=1}^{N-m}\left(\frac{1}{N-m-1}\sum_{\substack{j=1\\ j\neq i}}^{N-m} D_{i,j,m}\right) \qquad (9)$$

Repeating the same procedure from equation (7) and equation (8) for the vector $X_{m+1}(j)$, i.e., for dimension $(m+1)$, the function ϕ_{m+1} is obtained. Therefore, FuzzyEn can be estimated as

$$\text{FuzzyEn}\,(m,n,r,N) = \ln\phi_m(n,r) - \ln\phi_{m+1}(n,r) \qquad (10)$$

In this study, we applied the HVG and FuzzyEn to the solar quiet current, Sq(H), to investigate ionospheric chaos during SSW across the Europe and Africa sector. The computational parameters used for FuzzyEn analysis included an embedding dimension $(m = 1)$ and a tolerance threshold defined as r_1=0.2×std, where std represents the standard deviation of the time series X. Additionally, the argument exponent (pre-division) r_2=3 was applied, along with a time delay of τ=1. The window size used for the analysis was s=200.

The calculations were performed using Python with the EntropyHub library [EntropyHub. An Open-Source Toolkit for Entropic Time Series Analysis. Available online: https://www.entropyhub.xyz/ (accessed on 27 February 2024).] (version 0.2), which provides a reliable and standardized method for calculating FuzzyEn, ensuring that the results can be compared across different studies. EntropyHub integrates many established entropy methods into a single package, available for Python, MatLab, and Julia users. By utilizing this library, we ensured the consistency and reproducibility of our entropy calculations.

The solar quiet current time series during the SSW periods of 2009 (January-March) and 2021 (December 2020-February 2021) was transformed via the Horizontal Visibility Graph (HVG) to obtain a complex network representation. From this network, we derive a new node-degree time

series (maintaining the same length as the original). We then apply a sliding-window approach to calculate the Fuzzy Entropy on this new node-degree time series. Thus, while the HVG step converts the solar quiet current time series into a graph, the FuzzyEn measure is ultimately computed on the node-degree time series derived from that graph.

3. Observation and Results

A sample of solar quiet current $S_q(H)$ on 31st of March 2009 at Addis Ababa, Ethiopia is shown in Figure 6 (a-d). The panel (a) represents the time series of the solar quiet current derived in minutes. While the Horizontal Visibility Graph (HVG) step indeed yields a complex network representation, where a node-degree series of the solar quiet current is acquired. Panel (b) present node degree series, and by this it is some kind of detrending, effectively reflecting the node-degree sequence derived from the solar quiet time series data, which preserves the same length as the original time series. The panel (c) is the FuzzyEn depicting the entropy of the solar quiet current without applying HVG transformation. The result in panel (d) depicts the values of Fuzzy Entropy for the node degree distribution of this network representation for solar quiet current. We notice that the solar quiet current time series in panel (a) depicts an enhancement in magnitude during the peak noon periods in its daily variation, while at pre-noon and post-noon periods, a gradual increment and a decrease in the magnitude of the solar quiet current was observed. The results of the Fuzzy Entropy for the node-degree time series obtained after HVG transformation reveals a gradual decrease in entropy at noon-periods. While, at pre-noon and post-noon periods, the entropy depicts an increment. The node-degree sequence of solar quiet current, resulting from the HVG transformation highlight distinct entropy changes. These approach captures peaks and troughs in the time series of solar quiet current through horizontal visibility, thereby unveiling subtle fluctuations in the dynamical behavior of the ionospheric current system. When FuzzyEn is low,

it typically suggests more orderliness (less chaotic) behavior, whereas higher FuzzyEn values are associated with greater complexity or chaos. With this viewpoint, the HVG and FuzzyEn combination appears to reveal dynamical characteristic of the solar quiet current, including the potential emergence of chaotic behavior during the 2009 (January–March) and 2021 (December 2020–February 2021) SSW events.

The day-to-day latitudinal distribution of entropy across Europe and Africa sector in January 2009 is shown in Figure 7. The result depicts the entropy changes in color representation. The yellow color revealing the ranges of Fuzzy Entropy values between 1.2 and 1.4 indicates high entropy. This high entropy signifies the presence of ionospheric chaos in the ionospheric current system. The light blue color ranging at approximately 0.8~1.2 reveals a declining entropy value which indicates a transition from chaos to orderliness behavior in the ionospheric current system. While the deep blue color ranging at 0.6~0.8 depicts low entropy values. The low entropy reveals the presence of orderliness behavior in the ionospheric current system. We noticed that in the day-to-day latitudinal distribution of entropy across the stations in the European and African sector. Some days in January 2009 depicts the presence of ionospheric chaos at most of the stations shown in Figure 7. High entropy values were observed at stations situated at IZN, SUA, KIV, BOX and SOD on 1st, 4th, 8th, 10th, 14th, 18th-25th, and 28th-29th of January 2009. On 25th of January, a higher entropy values were depicted across all the stations in Europe and Africa sector. This observed feature of high entropy unveils the presence of chaotic behavior in the ionospheric dynamics of Europe and Africa sector. Low entropy values, signifying orderliness behavior in the dynamics of ionosphere was observed on 2nd, 3rd, 5th, 7th, 9th, 11th-13th, 15th-16th, 19th-20th, 23rd-24th, 26th-27th and 30th-31st of January. This observed low entropy are mostly domiciles in the Africa sector. In addition, our analysis revealed that lower entropy values were found on 3rd, 13th and

15th of January spreading across stations in Europe and Africa sector. This observed feature of low entropy across Europe and Africa sector reveals that the dynamics of the ionosphere on 13th and 15th of January exhibits a highly orderliness behavior.

We display the contour plots of the day-to-day latitudinal distribution of entropy on February 2009 in Figure 8. The changes in entropy depicts high values of Fuzzy Entropy revealing the presence of ionospheric chaos. This trend of high entropy values was noticed on 1st-2nd, 9th-10th, 17th of February signifying that the ionospheric dynamics of the aforementioned days are associated with chaotic behavior. In addition, 1st and 17th February exhibited a higher chaotic behavior that spread across all the stations investigated. This observation further strengthening the evident influence of SSW effects on the ionospheric dynamics on these dates. Notably, low entropy implying the presence of orderliness behavior in the dynamics of the ionosphere was obvious on 4th-8th, 11th-16th, 18th-26th of February 2009. However, 5th and 14th of February exhibited the lowest entropy values, revealing that the state of the ionosphere is exhibits strong orderliness behavior.

The day-to-day latitudinal distribution of entropy across the European and African sector on March 2009 is shown in Figure 9. Most of the Fuzzy entropy values are associated with low entropy. For instance, 1st-6th, 8th-18th, 20th-23rd, 25th-28th, and 31st of March depicts low changes in entropy in most of the stations. High entropy values associated with the presence of ionospheric chaos were found on 7th, and 29th-30th of March.

In 2021 SSW event analysis, because of unavailability of magnetic data in Africa sector especially in stations situated with the geographical longitude of $(26^0 - 40^0)$. Our analysis during 2021 SSW was restricted to only European sector. The result of the day-to-day latitudinal distribution of entropy across European sector is presented in Figure 10. We observed that the changes in entropy from 1st to 6th of December at the SOD, BOK and KIV stations reveals a consistently low entropy

values, indicating that the state of the ionosphere at these stations exhibits a consistent orderliness behavior during these periods. However, at SUA and IZN, a consistent high entropy values indicating the presence of ionospheric chaos was observed from 1st to 5th of December 2020. The day-to-day entropy changes on 7th-9th, and 11th-20th of December at SOD, BOX and KIV depicts a consistent high value of Fuzzy Entropy. Interestingly, SUA and IZN were consistently associated with a low entropy distribution from 8th to 22nd of December. This observed consistent feature of low entropy at SUA and IZN signifies that the influence of SSW effects on regional ionosphere of SUA and IZN manifest an orderliness behavior in the underly dynamics of ionosphere at this region. Furthermore, the possible emergence of ionospheric disturbances at SUA and IZN during those observed days highlights that perturbation due to 2021 SSW effect is minimal. A consistent decline feature from chaotic to orderliness behavior in the ionospheric dynamics was observed also at SOD, BOK, and KIV from 25th to 31st of December 2020, while SUA and IZN exhibited some features of ionospheric chaos on 30th and 31st of December.

For SSW of January 2021, the day-to-day latitudinal distribution of entropy across Europe sector is displayed in Figure 11. The latitudinal distribution depicts low entropy across the day-to-day observation in January. For instance, 1st-6th, 8th, 9th-10th, 13th, 17th, 19th-24th, 27th-29th and 30th-31st of January reveals low entropy values across the stations investigated in the Europe sector implying that the ionosphere at this region exhibits orderliness behavior in its underlying dynamics in most of the days consider in this study. Notably, high entropy, indicating the presence of ionospheric chaos was observed at SUA and IZN on 4th, 7th, 10th, 12th, and 13th, 16th of January 2021. In Figure 12, we depicted the day-to-day latitudinal distribution of entropy in February 2021 across Europe sector. The changes in entropy reveal high entropy, suggesting the presence of ionospheric chaos on 9th, 12th, 16th-18th, 21st, and also from 24th to 27th of February

2021 at SOD, BOX, SUA and IZN. In contrast, KIV consistently exhibited low values of entropy from 1st to 8th of February.

3.1 Ionospheric Chaos During Phases of 2009 SSW

Display in Figure 13 is the latitudinal distribution of entropy across Europe and Africa sector during different phases of 2009 SSW. The entropy analysis during the precondition phase of SSW depicts high entropy values across the stations in the European sector signifying that the precondition phase of 2009 SSW were associated with the emergence of ionospheric chaos. The observed features of high entropy values unveiling pronounced ionospheric chaos is found at SUA, KIV, BOX and SOD. This observation further reveals that the influence of SSW effects introduces an emergence of ionospheric perturbation in SUA, KIV, BOX and SOD at the preconditioning phase of 2009 SSW in Europe sector. It is noteworthy that the period from January to March 2009 were strongly associated with minimal activities of geomagnetic disturbance (see, Figure 2a). In the African sector, we noticed that the SSW preconditioning phase is characterized by a declining and low entropy values, implying that the regional ionosphere across Africa sector is revealing a suppression of orderliness behavior in the ionospheric dynamics at the preconditioning phase of 2009 SSW. A low entropy was seen at AAB, NAB and DES during the preconditioning phase signifying that the underlying dynamics of the ionosphere at AAB, NAB, and DES are exhibiting orderliness behaviour as the preconditioning phase of SSW emerges.

During the ascending phase of SSW, we observed also a low entropy values at stations in Africa sector up to IZN. However, high values of entropy implying the presence of ionospheric chaos were noticed at KIV, BOX, and SOD. The high entropy observed at KIV, BOX, and SOD during the ascending phase signifies that the influence of SSW effect on the regional ionosphere at KIV, BOX, and SOD is eminent. This suggests that SSW events significantly affect ionospheric

dynamics, leading to an increased chaotic pattern across Europe sector during the ascending phase of 2009 SSW. In the African sector, we observed that the region depicts low entropy values during ascending phase. This further signifies that the regional ionosphere in the Africa sector demonstrates orderliness behavior at the ascending phase of SSW.

During the peak phase of SSW 2009, evidence of ionospheric chaos was obvious at SOD, BOX, KIV, and SUA. The changes in Fuzzy entropy during this peak phase depicts high values, indicating significant disturbances in the ionosphere at Europe sector. A feature of declining entropy value was noticed to spread from IZN to DES. However, at around 4-10LT, low entropy values were seen at KRT, AAB and NAB. This observed declining entropy with a little feature of low entropy at KRT, AAB and NAB reveals that the regional ionosphere in Africa sector during the peak phase of SSW experience a suppression of orderliness behaviour. The suppression in orderliness behavior as SSW peak phases emerges further suggest that the regional ionosphere of Africa sector also experience a chaotic behavior. However, the European sector during the peak phase depicts higher degree of chaotic behavior. We suspect that the emergence of chaotic behavior due to SSW effect in Africa sector results in the suppression of orderliness behaviour.

At the descending phase of SSW, high entropy values associated with the presence of ionospheric chaos was evident at SOD, BOX, KIV, SUA, IZN. However, FYM, ASW, KRT, DES, LSK, and MPT reveals a declining entropy value, while AAB and NAB at around 8-16LT of the descending phase of SSW depicts low entropy values. The observed feature of declining entropy during the descending phase at stations situated in Africa sector signifies that the ionospheric dynamics exhibits a suppression in orderliness behaviour. This suppression of orderliness further suggests that the SSW effects during the descending phase introduce perturbation into regional ionosphere of Africa resulting to the suppression of orderliness behavior.

The after-SSW phase of 2009 also demonstrates a distribution of high values of entropy at SOD, BOX, KIV, SUA, SUA, and FYM. In the stations situated in Africa sector, low entropy begins to spreads from AAB to LSK while ASW, KRT and MPT depicts a declining value of entropy. The observed entropy changes during After-SSW phase signifies that SSW induced effect on Africa regional ionosphere begins to reduce. During the no-SSW phase, the degree of entropy associated with ionospheric chaos suppress at the following stations SOD, BOX, KIV, SUA and IZN. While a steady low entropy value was seen around ASW, KRT, AAB, NAB, DES, LSK, and MPT stations. This steady low entropy features seen during the no-SSW phase reveals that the regional ionosphere of Africa sector recovers back to its original dynamics.

3.2 Ionospheric chaos during phases of 2021 SSW

Shown in Figure 14 is the 2021 SSW latitudinal distribution of entropy across Europe sector at precondition, ascending, peak, descending, After-SSW and no-SSW phases. The Precondition phase at SOD, BOX, and KIV depicts high values of entropy signifying that ionospheric chaos is dominant during this period, while a declining and low entropy change was observed at IZN and SUA. The ascending, peak, descending and after SSW phases exhibit a consistent low entropy value in their latitudinal distribution, suggesting orderliness behavior in the ionosphere across SOD, BOX and KIV. In contrast, at SUA a consistent increase in entropy was evident. This consistent increase in entropy at SUA during all the phases of SSW implies that the ionospheric dynamics is consistently exhibiting chaotic behavior due to the influence of SSW.

4. Discussion of Results

The results unveil the dynamical characteristics in the solar quiet current $S_q(H)$ system during the 2009 and 2021 SSW events. Employing Horizontal Visibility Graph (HVG) and Fuzzy Entropy analysis, this study quantifies the chaotic and orderliness behavior exhibited by the ionospheric current system during SSW events across the European and African sectors. Ionospheric chaos is found to be most pronounced at European sector stations, particularly SUA, KIV, BOX, and SOD, demonstrating a higher degree of complexity and unpredictability in the ionospheric dynamics at this location. A notable dynamical feature of the ionospheric current system within the African sector was the consistent low entropy values observed at AAB, NAB, and DES, indicating the presence of orderliness behavior. In addition, our analysis revealed a transition from chaotic to orderliness behavior in the African sector as the stratospheric warming intensified. This transition was accompanied by a decline in entropy values. For instance, during the preconditioning phase of 2009 SSW, our results showed a decline in entropy values, signifying a shift towards orderliness behavior. Specifically, FYM, ASW, KRT, DES, LSK, and MPT exhibited declining entropy values, while AAB and NAB showed low entropy values around 9-11 LT. This decline in entropy during the preconditioning phase suggests that the SSW effects introduce perturbation to the regional ionosphere of the African sector, leading to a suppression of chaotic behavior, and transit to orderliness behavior in Africa sector. The European sector stations, comprising SOD, BOX, KIV, SUA, and IZN, exhibited elevated entropy values, signifying the presence of pronounced ionospheric chaos at preconditioning phase. During the ascending phase of the 2009 SSW, our analysis revealed that the European sector stations (SOD, BOX, KIV, SUA, and IZN) consistently exhibited high entropy values, indicating the presence of chaotic behavior. This pronounced ionospheric chaos suggests that the SSW-induced effects on the regional ionosphere of the

European sector are particularly significant. By comparison, the African sector exhibited more variable entropy measures, fluctuating between declining and low entropy values. Notably, Africa stations comprising of FYM, ASW, KRT, AAB, NAB, DES, LSK, and MPT showed low entropy values between 8-12 LT, while declining entropy values were observed at other local times. This divergence suggests that the ionosphere in the African sector is becoming more synchronized to orderliness behavior as the stratospheric temperature rises.

At the peak phase of 2009 SSW, our findings reveal an extended feature of converging orderliness behavior in the African sector. Notably, declining entropy values were observed at FYM, ASW, KRT, DES, LSK, and MPT, while low entropy values were evident at AAB and NAB. This converging orderliness behavior in the African sector during the SSW peak phase suggests that an external perturbation, induced by SSW effects, is influencing the regional ionosphere. This perturbation appears to suppress the chaotic behavior of the ionospheric current system in the African sector. Meanwhile, stations in the European sector, including SOD, BOX, KIV, and SUA, continued to exhibit chaotic behavior in their regional ionospheric dynamics. The descending phase of 2009 SSW, reveals a gradual recovery to orderliness behavior in the African sector. Low entropy values were evident, indicating a return to orderliness dynamics in the regional ionosphere. The recovery was characterized by low entropy values at KRT, AAB, NAB, and DES, while other African sector stations exhibited declining entropy values. This observed entropy distribution during the SSW's descending phase suggests that the African sector's regional ionosphere is reverting to orderliness behavior. Conversely, European sector stations, including IZN, SUA, KIV, BOX, and SOD, consistently displayed chaotic behavior.

During the after-SSW phase, a notable decline in entropy was observed at FYM, ASW, KRT, LSK, and MPT, implying a transition towards orderliness behavior at these stations. Additionally, low

entropy values were recorded from AAB to DES, signifying that ionosphere at AAB, NAB, and DES exhibiting orderliness behavior. On the other hand, European sector including SOD, BOX, KIV, SUA, and IZN continued to exhibit high entropy values suggesting a persistent ionospheric chaos. At the no-SSW phase, a notable expansion and spread of low entropy values were observed across all stations in the African sector. This entropy distribution pattern indicates that the regional ionosphere has fully recovered and the dynamics is reverted to orderliness behavior.

In the 2021 SSW, entropy analysis revealed distinct patterns of ionospheric chaos and orderliness across different stations. Initially, chaos increased at KIV, BOX, and SOD during the preconditioning phase, while SUA and IZN exhibited orderly behavior. In contrast, SOD, BOX, and KIV showed orderly behavior during the ascending, peak, and descending phases. However, chaos re-emerged at these stations during the after-SSW and no-SSW phases. Notably, SUA exhibited prominent chaotic behavior throughout the ascending, peak, descending, after, and no-SSW phases, highlighting the significant influence of SSW on ionospheric dynamics in certain regions of the European sector.

These findings of ionospheric chaos in most of the stations situated in the Europe sector reveals the evidence that the 2009 SSW effect indeed significantly influenced the ionospheric dynamics in European sector. Interestingly, during the 2009 SSW periods, the daily geomagnetic activities were mostly characterized by a planetary index of $K_p \leq 3$. However, we notice some certain days during the SSW periods, namely SSW 2009 (January 3, 19, 26, February 4, 14-15, 25, 28, March 13, and 24) and SSW 2021 (December 10, 21, 23, January 5, 6, 11, 24, 25, 27, February 2, 6, 12, 16, 20, 22, and 23), where there was a transient increase in the K_p values exceeding 3 within the three-hour intervals of K_p index. Notably, these transient emergence of K_p index exceeding 3 within few hours during SSW periods have a tendency of inducing a mild geomagnetic disturbance

during the SSW period, but may not be strong enough to be a dominant factor to influence ionospheric instability during SSW. The reason is that SSW events occur on a longer time scale, i.e. number of days compare to emergence of sudden geomagnetic disturbance within few hours. The contributing influence of SSW will be more significant than the transient disturbance of geomagnetic activities. While, we acknowledge that there is some transient geomagnetic disturbance revealed by K_p index during SSW periods. To address these possible geomagnetic disturbances indicated by the K_p index, all our daily solar quiet current derivation analysis during the SSW periods, we implement the subtraction of the geomagnetic storm index in minutes (SYM-H) from the H-component of the magnetic field to minimize the influence of geomagnetic disturbances. Therefore, the finding that ionospheric chaos been dominant in most stations located in the European sector provides additional evidence of the SSW's effect on the regional ionosphere in Europe sector. The presence of ionospheric chaos unveils the formation of large disturbances in the European sector owning to the impact of disruption on communication and navigation signals during SSW. We suspect that this observation of ionospheric chaos may be attributed to the enhancement of the solar and lunar migrating tides during SSWs, which influences the generation of electric fields through the E-region dynamo mechanism (Goncharenko et al., 2021; Pedatella et al., 2014; Siddiqui et al., 2018). Another contributing factor to the emergence of ionospheric chaos could be the Heliospheric plasma sheet's interaction with the Earth's magnetosphere which lead to significant magnetospheric processes like Relativistic Electron Dropout (RED) and EMIC wave generation. These processes have downstream effects on the lower atmospheric activities, potentially influencing weather pattern and climate through energy deposition and ionization changes (Tsurutani et al., 2016; Salminen et al., 2020)

556 The latitudinal distribution of entropy showed a transition from chaotic to orderliness behavior in
557 the African sector during the peak, descending, and after-SSW phases, highlighting the impact of
558 SSW on the regional ionosphere of Africa sector, which leads to suppresses of orderliness behavior.
559 This observed orderliness behavior in the Africa sector's ionosphere cannot be attributed to the
560 Equatorial Electrojet (EEJ), because EEJ is typically confined to the magnetic equation ($\pm 3^0$).
561 The result of our analysis reveals that the observed orderliness behavior extends beyond the
562 equatorial boundary. We suspect that the observed suppression and consistency in orderliness
563 behavior reflects that there is modification in Equatorial Ionization Anomaly (EIA) structure of
564 Africa sector due to the forcing effect from SSW and other external sources like Heliospheric
565 Plasma Sheet (HPS), magnetospheric processes (REDs, EMIC waves, etc.), and their impacts on
566 the lower atmosphere (via disturbance chains). The extension of orderliness behavior, associated
567 with low entropy values, spans from Addis Ababa (AAB) to Fayum (FYM) and Maputo (MPT),
568 indicating a significant alter in EIA structure driven by SSW influences. In our forthcoming
569 research, we will focus extensively on this orderliness behavior within the ionospheric current
570 system, particularly in the Africa equatorial region.

571

572 **5.0 Conclusion**

573 This study has unveiled the contributing influence of SSW on the regional ionosphere across
574 Europe and Africa by examining ionospheric chaos in the solar quiet current during the SSW
575 events of 2009 and 2021. These SSW events occurred during the solar minimum years of solar
576 cycle 24. The SSW was categorized according to the rising stratospheric temperature into six
577 phases namely precondition, ascending, peak, descending, after, and no-SSW phases. The study
578 covers 13 magnetometer stations across the Europe and Africa sector located within the

geographical longitude of 26° to 40° East. Magnetometer data obtained during the periods of SSW were used to derive time series of the solar quiet current, Sq(H). These solar quiet current time series were transformed into a network representation through the Horizontal Visibility Graph (HVG) approach and analyzed by Fuzzy Entropy to quantify the presence of ionospheric chaos during the periods of SSW. We found that the latitudinal distribution of entropy depicts high entropy indicating the presence of ionospheric chaos in most of the stations situated within the Europe sector compared to stations in the Africa sector. A consistent low entropy distribution unveiling the presence of orderliness behavior were found to be prominent in the Africa sector. This prevailing evidence of orderliness behavior in the Africa sector during SSW signifies that the contribution influence of SSW to the regional ionosphere of Africa sector manifest an orderliness behavior in its underlying dynamics. While, the pronounced features of ionospheric chaos associated with high entropy values found in the Europe sector. This ionospheric chaos unveils the evidence of significant effects of SSW on the regional ionosphere in Europe. Finally, we found that after the peak phase of SSW, the ionospheric chaos is more pronounced.

Code availability

The code is a collection of routines in MATLAB (MathWorks) and is available upon request to the corresponding author.

Data availability

The magnetometer data are publicly available and provided by Magnetic Data Acquisition System (MAGDAS) at the International Research Centre for Space and Planetary Environment Science, Fukuoka, Japan (http://magdas2.serc.kyushu-u.ac.jp/). The magnetometer can also be access at the International Real-time Magnetic Observatory Network (INTERMAGNET) (available online

601 at www.intermagnet.org). While the stratospheric temperature can be access from National
602 Oceanic and Atmospheric Administration (NOAA) (https://psl.noaa.gov/data/getpage/). The
603 planetary index are provided and access GFZ Indices of Global Geomagnetic Activity
604 (https://www.gfz-potsdam.de/Kp-index/). The data of disturbance storm time in minute resolution
605 (SYM-H) is available at the World Data Centre for Geomagnetism, Kyoto, Japan:
606 https://wdc.kugi.kyoto-u.ac.jp/, while the solar flux index are archived at the National Aeronautics
607 and Space Administration (NASA), Space Physics Facility: https://omniweb.gsfc.
608 nasa.gov/form/dx1.html

609 **Author contributions**

610 **IAO** developed the idea behind the problem being solved, supervise the project, analyzed the data;
611 developed the codes; and draft the manuscript; **VA** supervise the project, developed the codes,
612 analyzed the data and contribute to the drafting of the manuscript; **MN** supervise the project and
613 contribute to the drafting of the manuscript; **OOI, BOS, and OBO** contributes to the interpretation
614 and Discussion of results; **NAN and OOT** read and made useful comments to the manuscript.

615 **Competing interests**

616 Some authors are members of the editorial board of nonlinear processes in geophysics journal, and
617 the authors declare they have no conflict of interest.

618 **Acknowledgement**

619 The authors would like to appreciate the Magnetic Data Acquisition System (MAGDAS) for
620 providing the magnetometer data used for this research upon the request from the project leader of
621 MAGDAS/CPMIN observations Dr. A. Yosikawa. We also extend our gratitude to the
622 INTERMAGNET Networks for making available the magnetometer data across the globe.

References

Azami, H., Li, P., Arnold, S. E., Escudero, J., and Humeau-Heurtier, A.: Fuzzy entropy metrics for the analysis of biomedical signals: Assessment and comparison, IEEE Access, 7, 104833–104847, https://doi.org/10.1109/ACCESS.2019.2930625, 2019.

Baldwin, M. P., Ayarzagüena, B., Birner, T., Butchart, N., Butler, A. H., Charlton-Perez, A. J., Domeisen, D. I. V., Garfinkel, C. I., Garny, H., Gerber, E. P., Hegglin, M. I., Langematz, U., and Pedatella, N. M.: Sudden Stratospheric Warmings, Rev. Geophys., 59, 1–37, https://doi.org/10.1029/2020RG000708, 2021.

Barton, C. E. and Tarlowski, C. Z.: Geomagnetic, geocentric, and geodetic coordinate transformations, Comput. Geosci., 17, 669–678, https://doi.org/https://doi.org/10.1016/0098-3004(91)90038-F, 1991.

Bolaji, O. S., Oyeyemi, E. O., Owolabi, O. P., Yamazaki, Y., Rabiu, A. B., Okoh, D., Fujimoto, A., Amory-Mazaudier, C., Seemala, G. K., Yoshikawa, A., and Onanuga, O. K.: Solar quiet current response in the African sector due to a 2009 sudden stratospheric warming event, J. Geophys. Res. Sp. Phys., 121, 8055–8065, https://doi.org/10.1002/2016JA022857, 2016a.

Bolaji, O. S., Oyeyemi, E. O., Owolabi, O. P., Yamazaki, Y., Rabiu, A. B., Okoh, D., Fujimoto, A., Amory-Mazaudier, C., Seemala, G. K., Yoshikawa, A., and Onanuga, O. K.: Solar quiet current response in the African sector due to a 2009 sudden stratospheric warming event, J. Geophys. Res. Sp. Phys., 121, 8055–8065, https://doi.org/https://doi.org/10.1002/2016JA022857, 2016b.

Butler, A. H., Seidel, D. J., Hardiman, S. C., Butchart, N., Birner, T., and Match, A.: Defining sudden stratospheric warmings, Bull. Am. Meteorol. Soc., 96, 1913–1928, https://doi.org/10.1175/BAMS-D-13-00173.1, 2015.

Chau, J. L., Goncharenko, L. P., Fejer, B. G., and Liu, H. L.: Equatorial and low latitude ionospheric effects during sudden stratospheric warming events : Ionospheric effects during SSW events, Space Sci. Rev., 168, 385–417, https://doi.org/10.1007/s11214-011-9797-5, 2012.

Chen, W., Wang, Z., Xie, H., and Yu, W.: Characterization of Surface EMG Signal Based on Fuzzy Entropy, IEEE Trans. Neural Syst. Rehabil. Eng., 15, 266–272, https://doi.org/10.1109/TNSRE.2007.897025, 2007.

Conejero, J. A., Velichko, A., Garibo-i-Orts, Ò., Izotov, Y., and Pham, V. T.: Exploring the Entropy-Based Classification of Time Series Using Visibility Graphs from Chaotic Maps, Mathematics, 12, https://doi.org/10.3390/math12070938, 2024.

Dass, B., Tomar, V. P., and Kumar, K.: Fuzzy entropy with order and degree for intuitionistic fuzzy set, AIP Conf. Proc., 2142, https://doi.org/10.1063/1.5122619, 2019.

Fejer, B. G., Tracy, B. D., Olson, M. E., and Chau, J. L.: Enhanced lunar semidiurnal equatorial vertical plasma drifts during sudden stratospheric warmings, Geophys. Res. Lett., 38, https://doi.org/https://doi.org/10.1029/2011GL049788, 2011.

Gonçalves, B. A., Carpi, L., Rosso, O. A., and Ravetti, M. G.: Time series characterization via horizontal visibility graph and Information Theory, Phys. A Stat. Mech. its Appl., 464, 93–102, https://doi.org/10.1016/j.physa.2016.07.063, 2016.

Goncharenko, L. P., Chau, J. L., Liu, H.-L., and Coster, A. J.: Unexpected connections between the stratosphere and ionosphere, Geophys. Res. Lett., 37, https://doi.org/https://doi.org/10.1029/2010GL043125, 2010.

Goncharenko, L. P., Coster, A. J., Plumb, R. A., and Domeisen, D. I. V: The potential role of

stratospheric ozone in the stratosphere-ionosphere coupling during stratospheric warmings, Geophys. Res. Lett., 39, https://doi.org/https://doi.org/10.1029/2012GL051261, 2012.

Goncharenko, L. P., Harvey, V. L., Liu, H., and Pedatella, N. M.: Sudden Stratospheric Warming Impacts on the Ionosphere-Thermosphere System: A Review of Recent Progress, 369–400 pp., https://doi.org/10.1002/9781119815617.ch16, 2021.

Ishikawa, A. and Mieno, H.: The fuzzy entropy concept and its application, Fuzzy Sets Syst., 2, 113–123, https://doi.org/10.1016/0165-0114(79)90020-4, 1979.

Klimenko, M. V., Bessarab, F. S., Sukhodolov, T. V., Klimenko, V. V., Koren'kov, Y. N., Zakharenkova, I. E., Chirik, N. V., Vasil'ev, P. A., Kulyamin, D. V., Shmidt, K., Funke, B., and Rozanov, E. V.: Ionospheric Effects of the Sudden Stratospheric Warming in 2009: Results of Simulation with the First Version of the EAGLE Model, Russ. J. Phys. Chem. B, 12, 760–770, https://doi.org/10.1134/S1990793118040103, 2018.

Klimenko, M. V., Klimenko, V. V., Bessarab, F. S., Sukhodolov, T. V., Vasilev, P. A., Karpov, I. V., Korenkov, Y. N., Zakharenkova, I. E., Funke, B., and Rozanov, E. V.: Identification of the mechanisms responsible for anomalies in the tropical lower thermosphere/ionosphere caused by the January 2009 sudden stratospheric warming, J. Sp. Weather Sp. Clim., 9, https://doi.org/10.1051/swsc/2019037, 2019.

Li, C., Li, Z., Guan, L., Qi, P., Si, J., and Hao, B.: Measuring the complexity of chaotic time series by fuzzy entropy, ACM Int. Conf. Proceeding Ser., Part F1305, https://doi.org/10.1145/3102304.3102320, 2017.

Liu, H.-L., Wang, W., Richmond, A. D., and Roble, R. G.: Ionospheric variability due to planetary waves and tides for solar minimum conditions, J. Geophys. Res. Sp. Phys., 115,

https://doi.org/https://doi.org/10.1029/2009JA015188, 2010.

Liu, N., Jin, Y., He, Z., Yu, J., Li, K., and Cui, J.: Simultaneous Evolutions of Inner Magnetospheric Plasmaspheric Hiss and EMIC Waves Under the Influence of a Heliospheric Plasma Sheet, Geophys. Res. Lett., 49, 1–12, https://doi.org/10.1029/2022GL098798, 2022.

Luque, B., Lacasa, L., Ballesteros, F., and Luque, J.: Horizontal visibility graphs: Exact results for random time series, Phys. Rev. E, 80, 46103, https://doi.org/10.1103/PhysRevE.80.046103, 2009.

Maute, A., Hagan, M. E., Richmond, A. D., and Roble, R. G.: TIME-GCM study of the ionospheric equatorial vertical drift changes during the 2006 stratospheric sudden warming, J. Geophys. Res. Sp. Phys., 119, 1287–1305, https://doi.org/https://doi.org/10.1002/2013JA019490, 2014.

O'Pella, J.: Horizontal visibility graphs are uniquely determined by their directed degree sequence, Phys. A Stat. Mech. its Appl., 536, 120923, https://doi.org/10.1016/j.physa.2019.04.159, 2019.

Pedatella, N. M., Liu, H.-L., Sassi, F., Lei, J., Chau, J. L., and Zhang, X.: Ionosphere variability during the 2009 SSW: Influence of the lunar semidiurnal tide and mechanisms producing electron density variability, J. Geophys. Res. Sp. Phys., 119, 3828–3843, https://doi.org/https://doi.org/10.1002/2014JA019849, 2014.

Salminen, A., Asikainen, T., Maliniemi, V., and Mursula, K.: Dependence of Sudden Stratospheric Warmings on Internal and External Drivers, Geophys. Res. Lett., 47, 1–9, https://doi.org/10.1029/2019GL086444, 2020.

Siddiqui, T. A., Maute, A., Pedatella, N., Yamazaki, Y., Lühr, H., and Stolle, C.: On the variability of the semidiurnal solar and lunar tides of the equatorial electrojet during sudden stratospheric warmings, Ann. Geophys., 36, 1545–1562, https://doi.org/10.5194/angeo-36-1545-2018, 2018.

709 Tsurutani, B. T., Hajra, R., Tanimori, T., Takada, A., Bhanu, R., Mannucci, A. J., Lakhina, G. S.,
710 Kozyra, J. U., Shiokawa, K., Lee, L. C., Echer, E., Reddy, R. V., and Gonzalez, W. D.:
711 Heliospheric plasma sheet (HPS) impingement onto the magnetosphere as a cause of relativistic
712 electron dropouts (REDs) via coherent EMIC wave scattering with possible consequences for
713 climate change mechanisms, J. Geophys. Res. Sp. Phys., 121, 10,130-10,156,
714 https://doi.org/10.1002/2016JA022499, 2016.

715 Yamazaki, Y. and Maute, A.: Sq and EEJ—A Review on the Daily Variation of the Geomagnetic
716 Field Caused by Ionospheric Dynamo Currents, Space Sci. Rev., 206, 299–405,
717 https://doi.org/10.1007/s11214-016-0282-z, 2017.

718 Yamazaki, Y. and Richmond, A. D.: A theory of ionospheric response to upward-propagating
719 tides: Electrodynamic effects and tidal mixing effects, J. Geophys. Res. Sp. Phys., 118, 5891–
720 5905, https://doi.org/https://doi.org/10.1002/jgra.50487, 2013.

721 Yamazaki, Y., Richmond, A. D., Liu, H., Yumoto, K., and Tanaka, Y.: Sq current system during
722 stratospheric sudden warming events in 2006 and 2009, J. Geophys. Res. Sp. Phys., 117,
723 https://doi.org/https://doi.org/10.1029/2012JA018116, 2012b.

724 Yamazaki, Y., Yumoto, K., McNamara, D., Hirooka, T., Uozumi, T., Kitamura, K., Abe, S., and
725 Ikeda, A.: Ionospheric current system during sudden stratospheric warming events, J. Geophys.
726 Res. Sp. Phys., 117, 1–7, https://doi.org/10.1029/2011JA017453, 2012a.

727 Yamazaki, Y., Yumoto, K., Uozumi, T., and Cardinal, M. G.: Intensity variations of the equivalent
728 S current system along the 210° magnetic meridian, J. Geophys. Res. Sp. Phys., 116,
729 https://doi.org/https://doi.org/10.1029/2011JA016632, 2011.

730 Yamazaki, Y.: Large lunar tidal effects in the equatorial electrojet during northern winter and its

relation to stratospheric sudden warming events, J. Geophys. Res. Sp. Phys., 118, 7268–7271, https://doi.org/10.1002/2013JA019215, 2013.

Yamazaki, Y.: Solar and lunar ionospheric electrodynamic effects during stratospheric sudden warmings, J. Atmos. Solar-Terrestrial Phys., 119, 138–146, https://doi.org/10.1016/j.jastp.2014.08.001, 2014.

Zou, Y., Donner, R. V., Marwan, N., Donges, J. F., and Kurths, J.: Complex network approaches to nonlinear time series analysis, Phys. Rep., 787, 1–97, https://doi.org/10.1016/j.physrep.2018.10.005, 2019.

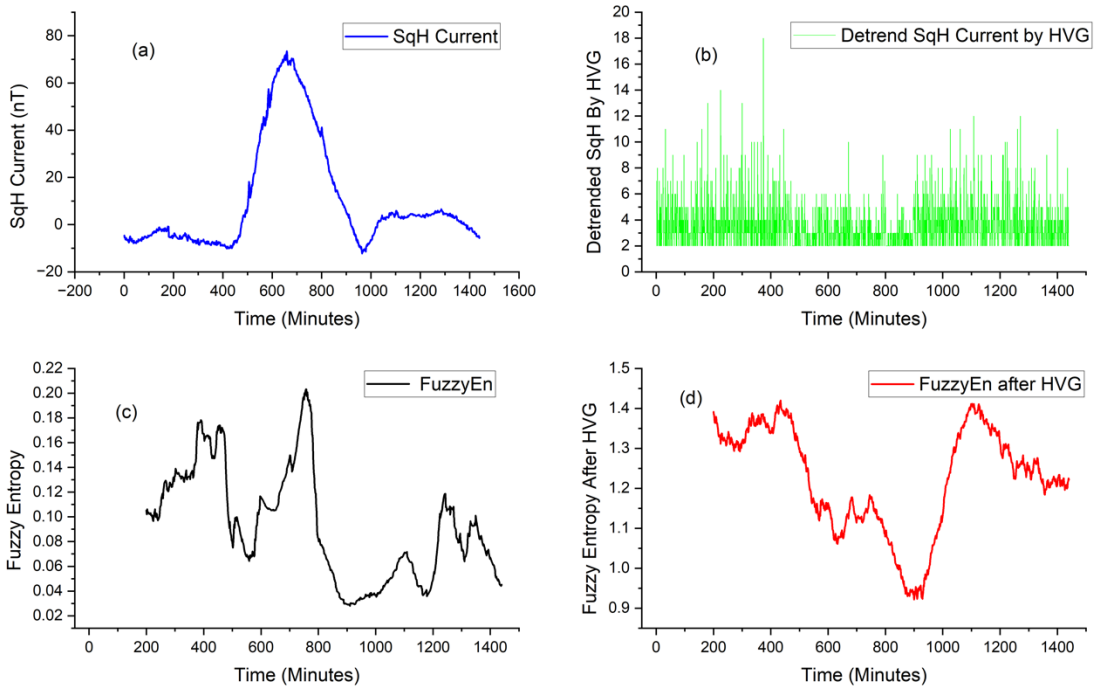

744

745 **Figure 6**: The sample of solar quiet current Sq(H) on 31st of March 2009 at Addis Ababa, Ethiopa:
746 (a) The time series of solar quiet current, Sq(H) derived in minutes, (b) The detrended time series
747 of solar quiet current transformed through Horizontal Visibility Graph (HVG), (c) The changes in
748 Fuzzy Entropy of solar quiet current without HVG transformation, (d) The changes in Fuzzy
749 Entropy of solar quiet current with HVG transformation.

750

751

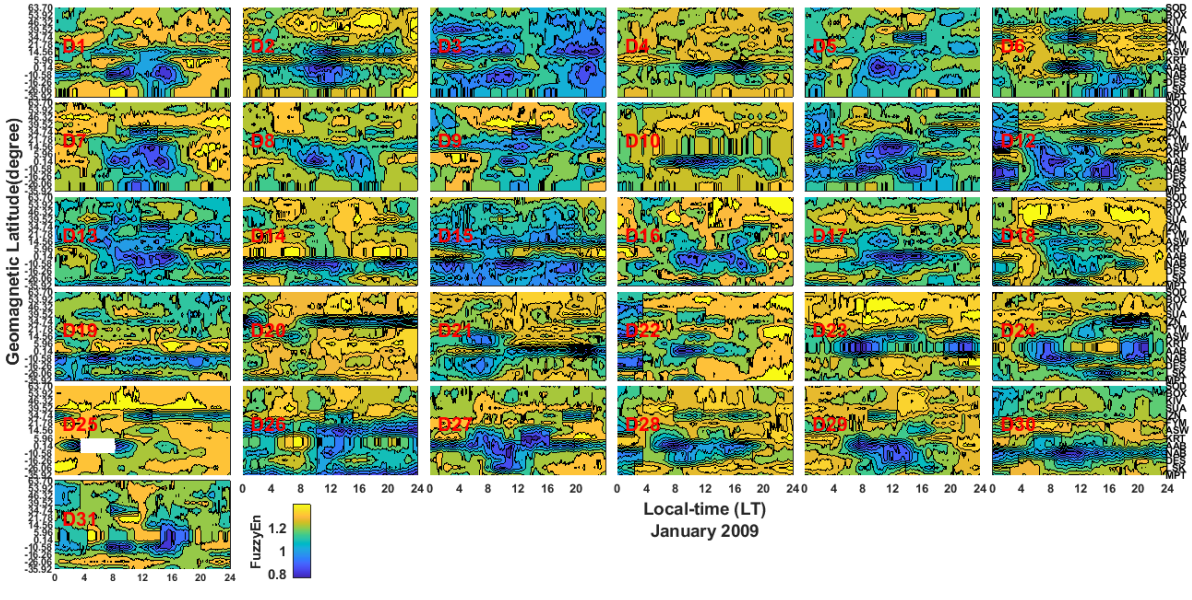

752

753 **Figure 7:** The Day-to-Day latitudinal Distribution of Fuzzy Entropy across Europe-Africa sector

754 on January 2009

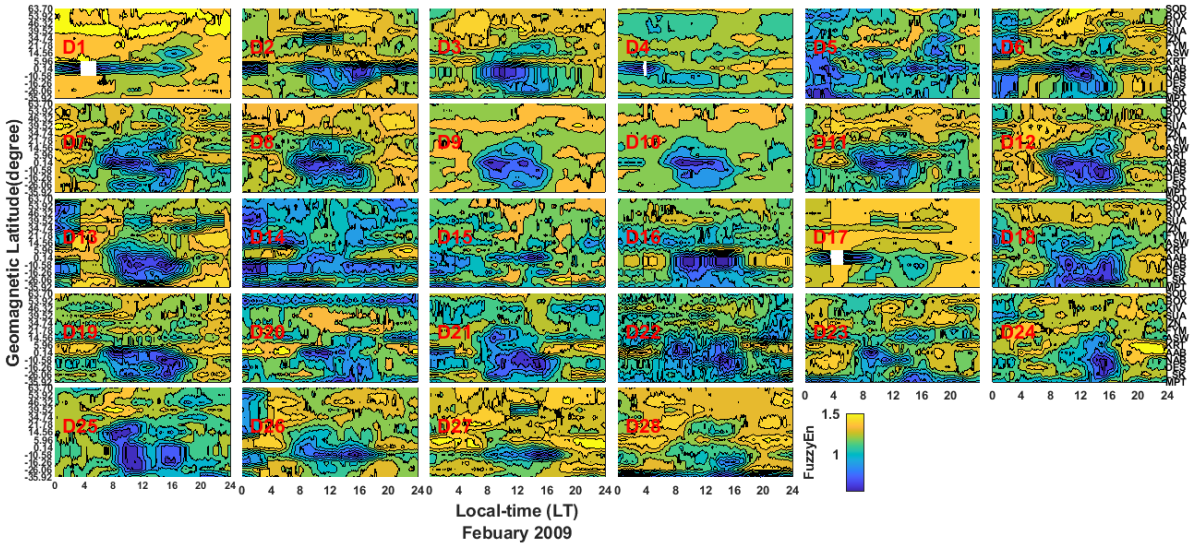

755

756 **Figure 8:** The Day-to-Day latitudinal Distribution of Fuzzy Entropy across Europe-Africa sector

757 on February 2009.

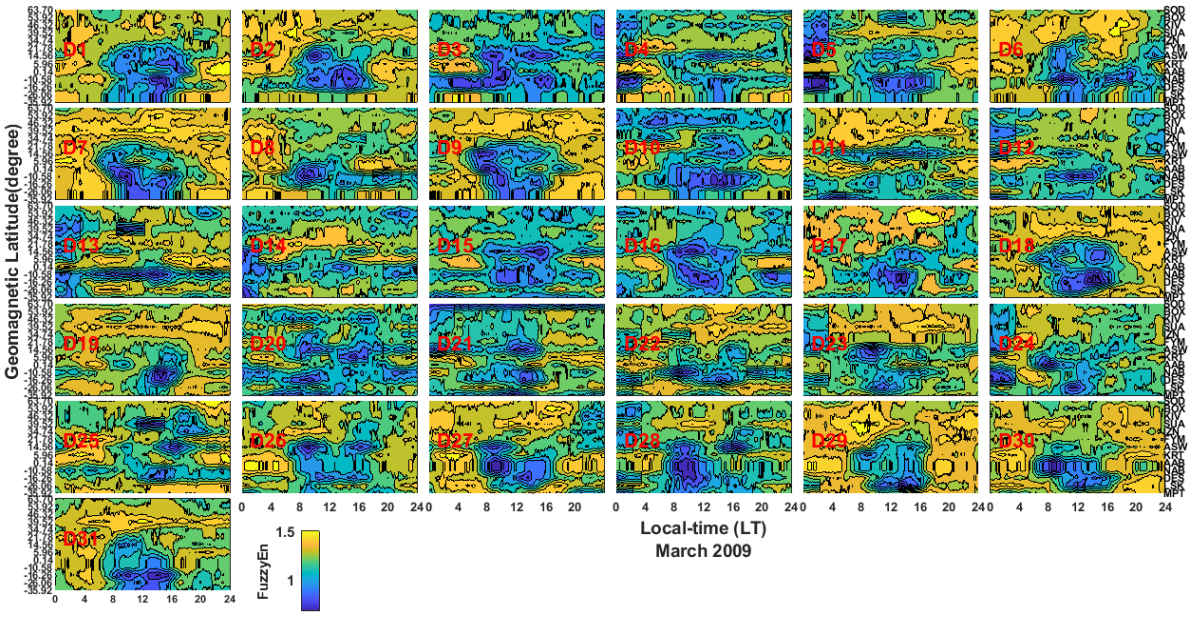

758

759 **Figure 9:** The Day-to-Day latitudinal Distribution of Fuzzy Entropy across Europe-Africa sector

760 on March 2009

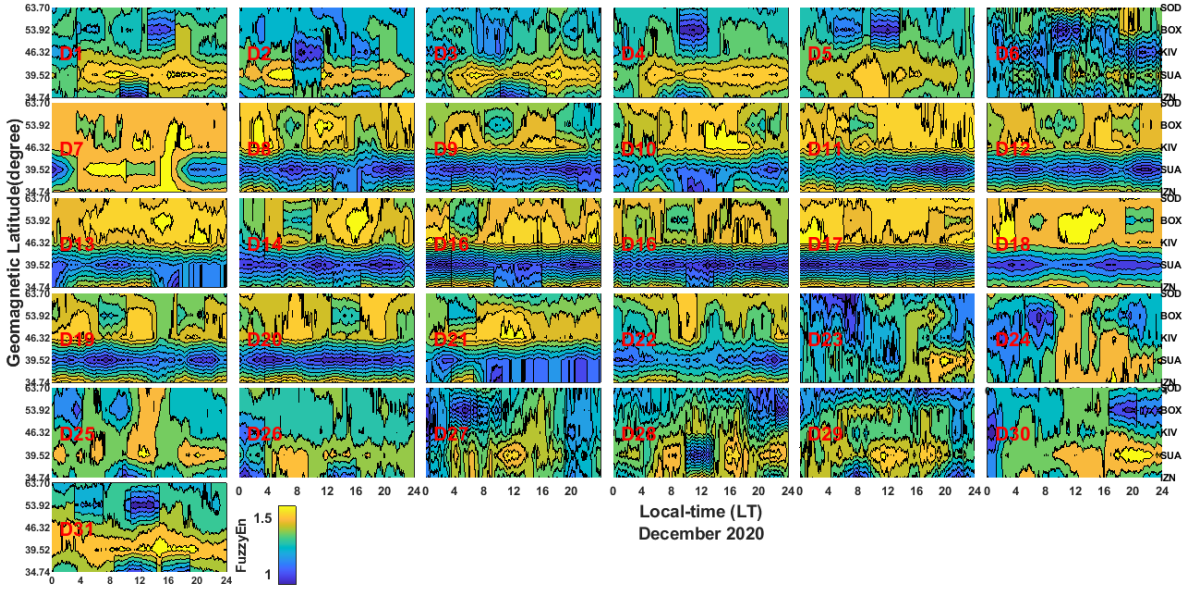

761

762 **Figure 10:** The Day-to-Day latitudinal Distribution of Fuzzy Entropy across Europe sector on

763 December 2020

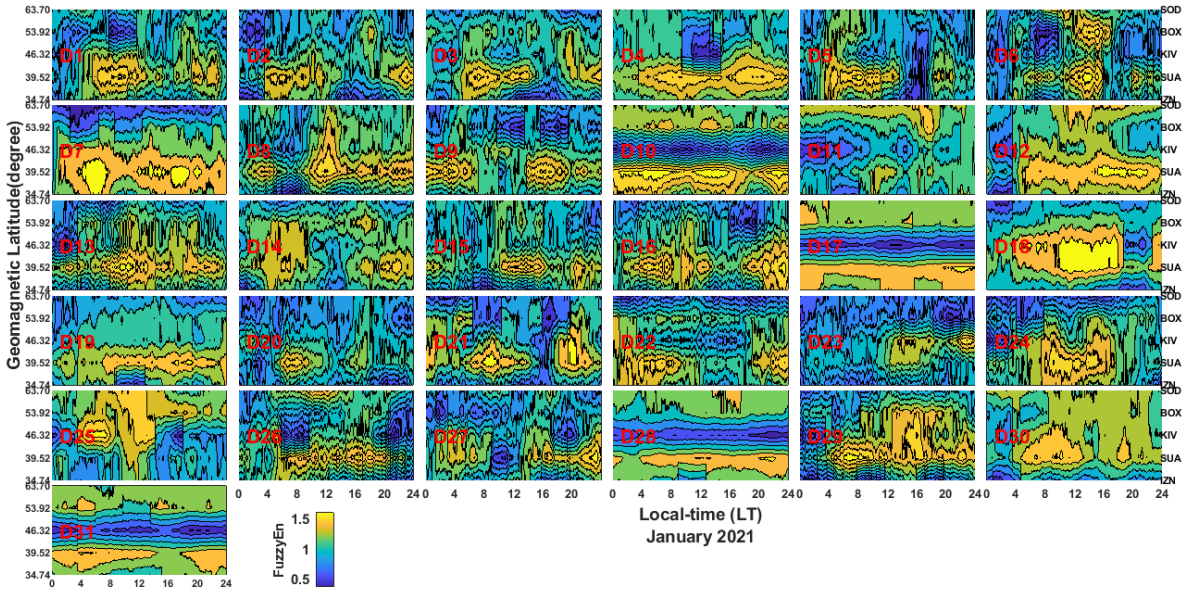

764

765 **Figure 11:** The Day-to-Day latitudinal Distribution of Fuzzy Entropy across Europe sector on

766 January 2021.

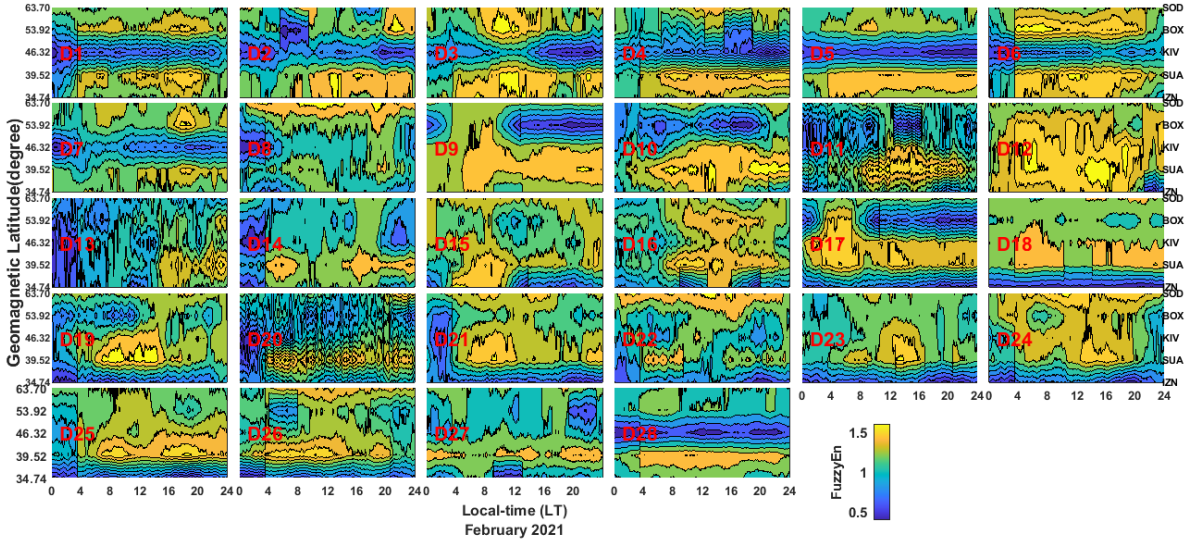

767

768 **Figure 12:** The Day-to-Day latitudinal Distribution of Fuzzy Entropy across Europe sector on

769 February 2021.

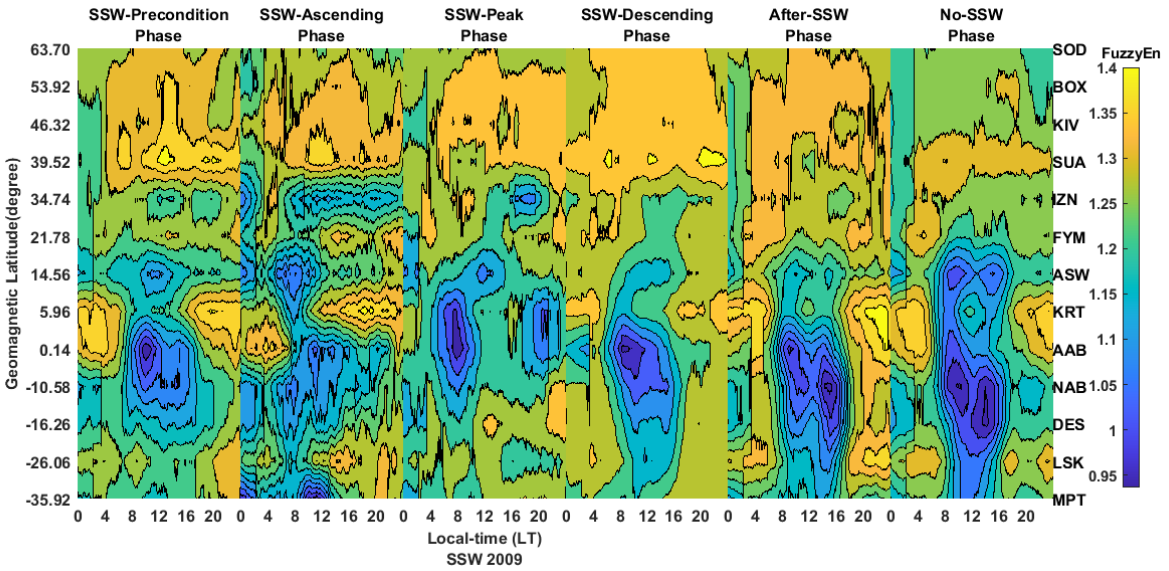

770

771 **Figure 13:** The latitudinal distribution of Fuzzy Entropy across Europe-Africa sector during the

772 phases of 2009 SSW.

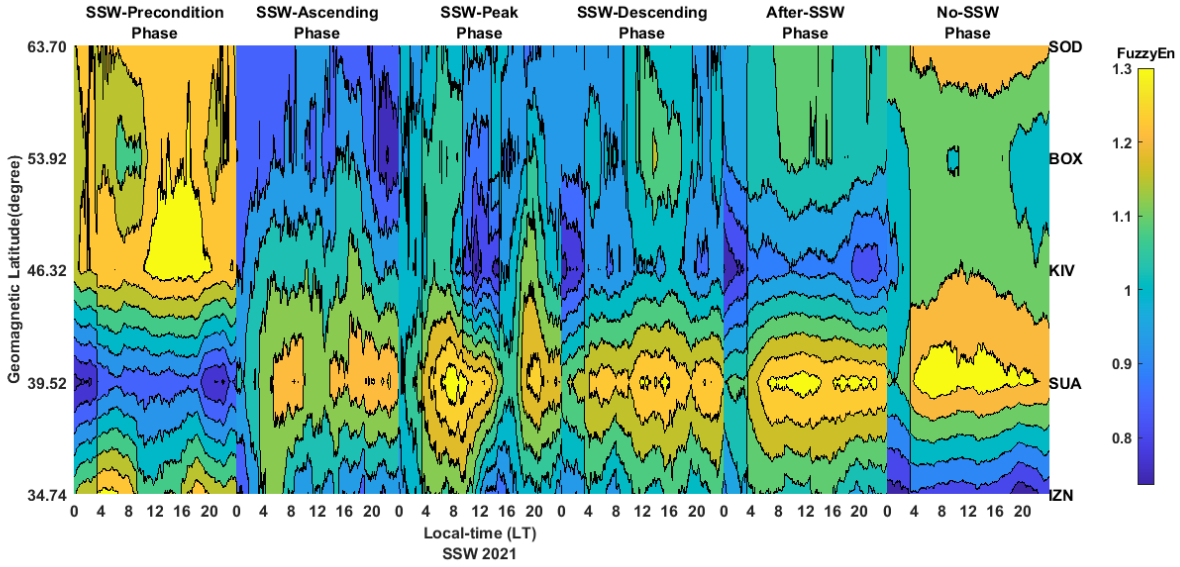

773

774 **Figure 14:** The latitudinal distribution of Fuzzy Entropy across Europe sector during the phases

775 of 2021 SSW.